THE ORIGIN OF THE MOST IRON-POOR STAR

S. MARASSI[1], G. CHIAKI[2], R. SCHNEIDER[1], M. LIMONGI[1,3], K. OMUKAI[4], T. NOZAWA[5], A. CHIEFFI[6], AND N. YOSHIDA[2,7]

[1] INAF/Osservatorio Astronomico di Roma, Via di Frascati 33, I-00040 Monteporzio, Italy; stefania.marassi@oa-roma.inaf.it
[2] Department of Physics, Graduate School of Science, The University of Tokyo, 7-3-1 Hongo, Bunkyo, Tokyo 113-0033, Japan
[3] Kavli Institute for the Physics and Mathematics of the Universe, Todai Institutes for Advanced Study, The University of Tokyo, Kashiwa 277-8583, Japan
[4] Astronomical Institute, Tohoku University, Sendai 980-8578, Japan
[5] National Astronomical Observatory of Japan, Mitaka, Tokyo 181-8588, Japan
[6] INAF/IASF, Via Fosso del Cavaliere 100, I-00133 Roma, Italy
[7] National Astronomical Observatory of Japan, Mitaka, Tokyo 181-8588, Japan
Received 2014 May 7; accepted 2014 August 8; published 2014 September 26

ABSTRACT

We investigate the origin of carbon-enhanced metal-poor (CEMP) stars starting from the recently discovered $[Fe/H] < -7.1$ star SMSS J031300. We show that the elemental abundances observed on the surface of SMSS J031300 can be well fit by the yields of faint, metal-free, supernovae (SNe). Using properly calibrated faint SN explosion models, we study, for the first time, the formation of dust grains in such carbon-rich, iron-poor SN ejecta. Calculations are performed assuming both unmixed and uniformly mixed ejecta and taking into account the partial destruction by the SN reverse shock. We find that, due to the paucity of refractory elements beside carbon, amorphous carbon is the only grain species to form, with carbon condensation efficiencies that range between (0.15 and 0.84), resulting in dust yields in the range (0.025–2.25) $M_\odot$. We follow the collapse and fragmentation of a star-forming cloud enriched by the products of these faint SN explosions and we explore the role played by fine structure line cooling and dust cooling. We show that even if grain growth during the collapse has a minor effect of the dust-to-gas ratio, due to C depletion into CO molecules at an early stage of the collapse, the formation of CEMP low-mass stars, such as SMSS J031300, could be triggered by dust cooling and fragmentation. A comparison between model predictions and observations of a sample of C-normal and C-rich metal-poor stars supports the idea that a single common pathway may be responsible for the formation of the first low-mass stars.

Key words: dust, extinction – ISM: general – ISM: supernova remnants – supernovae: general

Online-only material: color figures

1. INTRODUCTION

Stellar archaeology of the most metal-poor stars observed in the halo of our Galaxy provides valuable insights on the star formation and chemical enrichment histories at high redshifts. The observed surface elemental abundances and the metallicity distribution function of Galactic halo stars shed light on the nature and properties of the first supernovae (SNe; Population III SNe) that pollute the interstellar medium (ISM) with the first metals and dust grains.

Galactic halo metal-poor stars have a well-defined abundance pattern at $[Fe/H] < -2.5$ (Cayrel et al. 2004) that can be reasonably well reproduced by theoretical yields of Population III core-collapse SNe with progenitor masses in the range 10–100 $M_\odot$ (Heger & Woosley 2010, Limongi & Chieffi 2012). An exception are the so-called carbon-enhanced extremely metal-poor stars (CEMP, defined as those with $[C/Fe] > +1$ (Beers & Christlieb 2005), which comprise a fraction of $\sim$10%–20% of metal-poor stars at $[Fe/H] < -2$; Yong et al. 2013b). Interestingly, the observed fraction of C-rich metal-poor stars increases with decreasing iron abundance and, at $[Fe/H] < -4.5$, four out of the five stars currently known are CEMP, including the recently discovered SMSS J031300.36-670839.3 (hereafter SMSS J031300) with $[Fe/H] < -7.1$ (Keller et al. 2014).

A number of theoretical scenarios have been proposed to explain the origin of CEMP stars, invoking mass transfer in Population III binary systems (Suda et al. 2004, Masseron et al. 2010, Campbell et al. 2010), formation from material enriched in stellar winds of rotating massive and intermediate mass Population III stars (Meynet et al. 2006, Meynet et al.

2010, Hirschi 2007), or in the ejecta of Population III SNe in which mixing was minimal and fallback was large. In the latter model, the small iron abundance thus reflects the fact that in these so-called "faint" SNe iron was made, but failed to be mixed sufficiently far out to be ejected (Umeda & Nomoto 2003). Alternatively, the large C/Fe could result from multiple generations of SNe, where the ejecta of a "normal" SN is combined with that from a low-energy SN in which only the outer layers are ejected (Limongi & Chieffi 2003), or from a jet-induced SN explosion (Tominaga et al. 2007).

Understanding the origin of CEMP stars is complicated by the fact that these do not form a homogeneous group and show various heavy-element abundance patterns: depending on the level of enrichment of neutron capture elements formed by the "s" or "r" processes, these fall in different sub-classes (CEMP-no, CEMP-rs, CEMP-s; Beers & Christlieb 2005). Generally, CEMP-s and CEMP-rs stars have abundance patterns that suggest mass transfer from companion AGB stars (Masseron et al. 2010); indeed, most of the stars falling in these sub-classes are members of binary systems (Lucatello et al. 2005). However, at $[Fe/H] < -3$, 90% of CEMPs are CEMP-no stars, which do not show large enhancements of heavy neutron capture elements (Aoki et al. 2010). Using a homogeneous chemical analysis of 190 metal-poor stars (Yong et al. 2013a). Norris et al. (2013) have recently investigated a sample of CEMP-no stars with $[Fe/H] < -3$. They conclude that the observed chemical abundances are best explained by models that invoke the nucleosynthesis of Population III SNe with mixing and fallback, of rotating massive and intermediate mass stars and of SNe with relativistic jets.

Similar conclusions have been drawn by Keller et al. (2014) in their discovery paper of SMSS J031300, a Galactic halo star with only an upper limit on the iron abundance of [Fe/H] < −7.1. The observed abundance pattern of this extremely iron-deficient star is optimally matched by the nucleosynthetic yields of a 60 $M_\odot$ Population III SN with a small amount of ejecta mixing due to Rayleigh-Taylor instabilities, followed by extensive fallback of material onto the black hole remnant (Joggerst et al. 2009, Heger & Woosley 2010). They argue against a jet-like explosion as this would lower the [Mg/Fe] below that observed; in addition, rapidly rotating star models are also disfavored by the low upper limit on N compared to C (Keller et al. 2014).

A general conclusion of the above analyses is that below [Fe/H] ∼ −3 there appear to be two populations of stars, carbon-normal and carbon-rich, whose observed elemental abundances reflect the nucleosynthetic products of "normal" and "faint" Population III SNe, respectively. The different composition in the material out of which these low-mass stars form have stimulated the hypothesis that their formation relies on two different cooling channels (Norris et al. 2013): fine-structure-line cooling and dust cooling. In particular, C-rich stars form from C-enriched material where gas cooling and fragmentation is dominated by C II (and eventually O I) fine structure lines (Bromm & Loeb 2003).

Frebel et al. (2007) have introduced the so-called transition discriminant $D_{\rm trans} = \log(10^{[\rm C/H]} + 0.9 \times 10^{[\rm O/H]})$ and predicted that metal-poor stars forming through this mechanism must have $D_{\rm trans} > -3.5 \pm 0.2$ (Frebel & Norris 2013). They predict that metal-poor stars forming through this mechanism must have $D_{\rm trans} > -3.5 \pm 0.2$. Nearly all stars satisfy this criterion with the exception of SDSS J1029151+1729 (Caffau et al. 2011). This is a carbon-normal star with [Fe/H] = −4.99 and a solar-like chemical abundance pattern, leading to a total metallicity of $Z = 4.5 \times 10^{-5} Z_\odot$ and representing the most chemically pristine object currently known. The origin of the star has been investigated by Schneider et al. (2012b), who suggest that the observed abundance pattern of SDSS J1029151 can be well matched by yields of "normal" Population III SNe with 20 and 35 $M_\odot$; the mass of dust formed in these SN ejecta is enough to satisfy the minimal conditions to activate dust-induced fragmentation, which require the gas to be pre-enriched above a critical dust-to-gas mass ratio $\mathcal{D}_{\rm cr} = [2.6\text{–}6.3] \times 10^{-9}$, with the spread reflecting the dependence on the grain properties (Schneider et al. 2003, 2010, 2012a). Note that even if dust formation in the first SNe is less efficient or if strong dust destruction by the SN reverse shock occurs, grain growth during the collapse of the parent gas cloud is sufficiently rapid to activate dust cooling and fragmentation (Nozawa et al. 2012; Chiaki et al. 2013).

In principle, the values $\mathcal{D}_{\rm cr} = [2.6\text{–}6.3] \times 10^{-9}$ and $D_{\rm trans} > -3.5 \pm 0.2$ could provide a way to test dust cooling and on fine-structure-line cooling against the observations. This has been recently explored by Ji et al. (2014), who, however, make the a priori assumption that dust is made by silicates. In this way they estimate the critical silicate abundance, which corresponds to $\mathcal{D}_{\rm cr}$, and compare these values to chemical abundances of metal-poor stars, with [Fe/H] < −4. They find that the stars exhibit either high carbon with low silicon abundances or the reverse. A silicate dust scenario would thus support the hypothesis that the earliest low-mass star formation in the most metal-poor regime may have proceeded by means of two distinct cooling pathways: fine-structure line cooling and dust cooling.

Here we intend to investigate the origin of CEMP-no stars, and in particular of the recently discovered most iron-deficient

member of this class, SMSS J031300 (Keller et al. 2014). For the first time, we consider the formation of dust in faint Population III SN ejecta. Our aim is to verify if dust can form in these C-rich, iron-poor ejecta, and what is the relative role of fine-structure-line cooling and dust cooling in the collapse of material enriched by these explosions.

Having this goal in mind, we first compare the observed abundances of SMSS J031300 with the nucleosynthetic yields of model Population III SNe that range in progenitor mass, internal mixing, and explosion energy (extent of fallback; Section 2). We perform dust calculation in the ejecta of the selected SN models with a revised version of the Bianchi & Schneider (2007) model, which includes an improved, non-steady-state, molecular network, updated radiative association reactions for CO, SiO, C_2, and O_2 molecules, and formation/destruction processes between molecules (Marassi et al. 2014; S. Marassi et al. 2014, in preparation; Section 3). We follow the collapse of a gas cloud assuming that the newly formed dust and the metals present in the ejecta are uniformly mixed into the collapsing cloud with the same total metallicity that is observed on the surface of SMSS J031300 and verify under which conditions the formation of low-mass star is enabled (Section 4). Finally, we discuss the implications of our results for the origin of the first low-mass stars in the universe (Section 5).

2. FAINT SUPERNOVA PROGENITORS

Our aim here is to identify a set of plausible Population III SN models that may have polluted the birth cloud of SMSS J031300. The procedure that we follow is to minimize the scatter with the observed abundance pattern, adopting the chemical yields produced by a set of Population III core-collapse SN models with mixing and fallback.

We refer the interested reader to Limongi & Chieffi (2012) for a thorough presentation of the models. Similarly to what has been done in Schneider et al. (2012b), we consider a set of models that extends in mass between 13 and 80 $M_\odot$, which appear to be consistent with the mass range found by the most recent simulations of first star formation (Hirano et al. 2014). These models have been followed from the pre-main-sequence phase up to the onset of the iron core collapse by means of the FRANEC stellar evolutionary code. The initial composition is set to the pristine Big Bang nucleosynthesis ($Y = 0.23$) and mass loss is switched off during all the evolutionary stages.

The explosive nucleosynthesis has been computed in the framework of the induced explosion (Limongi & Chieffi 2006) approximation. For each progenitor model, we identify a combination of mixing and fallback that provides the best-fit to the observed elemental abundance ratios (or upper limits) on the surface of SMSS J031300. The observational data points are shown in Figure 1: black points with arrows show the inferred one-dimensional/three-dimensional (1D/3D) model atmosphere upper limits and the filled black dots with error bars are the 1D/3D model atmosphere detections (see Keller et al. 2014 for a description of the model atmosphere used for the abundance analysis). Among the three elements that have been detected—C, Mg, and Ca—we show the elemental abundances relative to Ca.

The low upper limit on [N/Ca] disfavors SN progenitors with initial masses in the range [20–35] $M_\odot$. In fact, their evolution leads to comparable C and N abundances in the ejecta (see Figure 7 and the discussion in Limongi & Chieffi 2012), in contrast to the observed pattern in SMSS J031300. Hence, we include in the analysis SN progenitors with initial masses equal
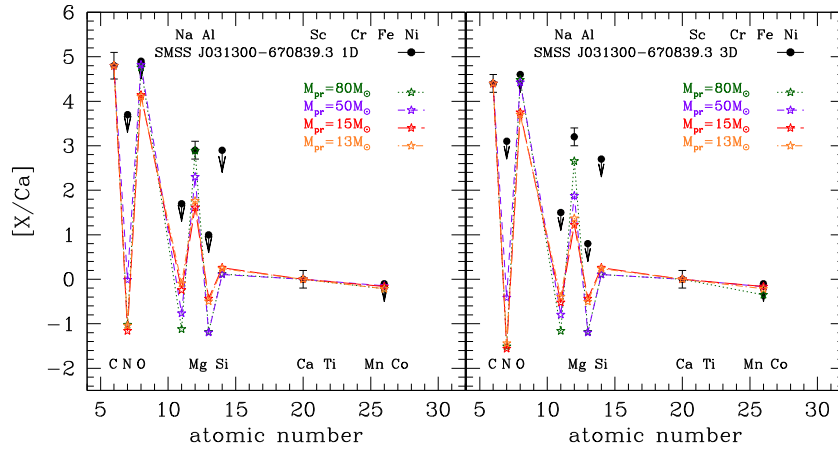
Figure 1. Comparison between the observed element abundance ratios of the star SMSS J031300 and the chemical yields of a Population III faint SN with progenitor masses of 13, 15, 50, and 80 $M_\odot$. Mixing and fallback are chosen so as to minimize the scatter with the observations using a 1D (left panel) or 3D (right panel) model atmosphere (black points). Dots with arrows show upper limits and filled points with errorbars indicate the detections, where an error of 0.1 (0.2) has been associated to the observed Ca and Mg (C) abundances.

(A color version of this figure is available in the online journal.)

to 13, 15, 50, and 80 $M_\odot$. For each of these models, we have applied the optimal combination of mixing (set by minimum and maximum mass coordinates within which the mass of each element is uniformly mixed in the ejecta) and fallback (set by the mass-cut) that minimizes the scatter with the observed abundance pattern. Since the elemental abundances inferred from the analysis using 1D or 3D model atmospheres lead to sensible differences in the observed abundances (or upper limits) of elements that are critical for the resulting dust mass, such as C, O, and Mg, for each progenitor mass we have independently inferred best-fit models using 1D and 3D observed elemental abundances. The resulting models are shown by the starred points joined with dotted lines in Figure 1. It is clear from the figure that while all the models show an overall agreement with the observed abundance pattern, it is hard to simultaneously accommodate the upper limit on [O/Ca] and the detected [Mg/Ca]; this is particularly true for low-mass progenitors, whose evolution leads to a lower [Mg/O] in the ejecta. The best-fit model appears to be the most massive progenitor with 80 $M_\odot$: adopting the abundance pattern inferred from 1D atmosphere models, the predicted ejecta composition is compatible with all the data points. This is not true, however, when the 3D data points are considered (see the right panel in Figure 1) as the more stringent upper limit on [O/Ca] and the larger [Mg/Ca] cannot be reproduced. Note that in Keller et al. (2014) the model that provides the optimal match to the observed abundance pattern is a 1.8×10^{51} erg explosion of a 60 $M_\odot$ star of primordial composition with a small amount of ejecta mixing and a strong fallback. These properties closely resemble our best-fit model and indeed the predicted [Mg/H] falls below the observational data point (see Figure 3 in Keller et al. 2014).

Table 1 summarizes the main properties of the SN progenitors. For all models, we choose the interval of mixing and mass-cut to reproduce the observed [C/Ca] and maximize the [Mg/Ca], getting as close as possible to the observed value without exceeding the [O/Ca] and [Fe/Ca] upper limits. We find that for all but the most massive model, the ejecta composition is insensitive to the reference set of observed abundances, whether derived with 1D or 3D model atmosphere (the values quoted in the table refer to the 3D set). Conversely, the chemical structure of the 80 $M_\odot$ progenitor, characterized by a more extended Mg shell, leads to [O/Ca] and [C/Ca] abundance ratios

that are more sensitive to the mixing and fallback prescription adopted. As a result, in Table 1 we show the ejecta composition for both sets of observed abundances and refer to the models as 80 $M_\odot$-1D or 80 $M_\odot$-3D.

3. DUST FORMATION IN FAINT SN

The formation of dust in SN ejecta has been modeled following either classical nucleation theory (CNT; Todini & Ferrara 2001; Nozawa & Kozasa 2003; Nozawa et al. 2010; Bianchi & Schneider 2007, and references therein) or a chemical kinetic approach (Cherchneff & Dwek 2009, 2010; Sarangi & Cherchneff 2013). As recently pointed out in Cherchneff & Dwek (2009, 2010) and Sarangi & Cherchneff (2013), these methods lead to different estimates of the mass and composition of newly formed dust due to the questionable applicability of the standard CNT in SN ejecta (Donn & Nuth 1985) and to non-equilibrium chemical processes related to the formation/destruction of molecules (Cherchneff & Dwek 2009). Recently, Paquette & Nuth (2011) have shown that the assumption of chemical equilibrium at nucleation, adopted within CNT, has only a minor effect on the grain mass and size distribution. In addition, Nozawa & Kozasa (2013) have demonstrated that a steady-state nucleation rate is a good approximation in SN ejecta, at least until the collisional timescales of the key molecule is much smaller than the timescale with which the supersaturation ratio increases.

Here we follow CNT to compute the nucleation and accretion of dust species using a previously developed code that has been applied to core-collapse (Todini & Ferrara 2001; Bianchi & Schneider 2007) and pair-instability SNe (Schneider et al. 2004) and that can successfully reproduce observational data of SNe and young SN remnants (Schneider et al. 2014; Valiante & Schneider 2014).

For the present study, the code has been improved allowing to solve the non-steady-state formation of important molecular species, such as CO, O_2, C_2, and SiO. A full description of the upgraded molecular network with the reactions rates will be given in Marassi et al. (2014). Here we restrict the discussion to those aspects that are relevant for carbon dust formation in faint SN ejecta. It is important to stress that the upgraded molecular network has been tested against the results obtained by chemical

Table 1

Properties of Faint SN Progenitors, Including the Explosion Energy [10^{51} erg], the Ejecta Velocity (km s^{-1}), the Gas Number Density (cm^{-3}), and the Radius of He Core, R_0 (cm) at $t = t_0$ (s) when Adiabatic Expansion Starts (see Text); in Addition, we also Show the Helium Core Mass, the Mass of the Ejecta, and the Initial Masses of the Elemental Yields that are Observed on the Surface of SMSS J031300, C, N, O, Na, Mg, Al, Si, Ca, and Fe ($M_\odot$)

	13 $M_\odot$	15 $M_\odot$	50 $M_\odot$	80 $M_\odot$	80 $M_\odot$	80 $M_\odot$	80 $M_\odot$
	3D	3D	3D	3D	1D	1D-A	1D-B
$E_{\rm exp}$	0.5	0.7	2.6	5.2	5.2	5.2	5.2
$M_{\rm He_{core}}$	2.81	3.40	18.11	31.94	31.94	31.94	31.94
$M_{\rm cut}$	1.7	2.1	11	22.5	24	24	24
$v_{\rm eje}$	2722	3011	3344	3891	3943	3943	3943
$M_{\rm eje}$	11.3	12.9	39	57.5	56	56	56
R_0	2.65×10^{14}	2.44×10^{14}	2.51×10^{14}	4.78×10^{14}	4.78×10^{14}	2.29×10^{14}	4.57×10^{14}
t_0	2.11×10^{6}	1.78×10^{6}	3.12×10^{6}	4.14×10^{6}	4.14×10^{6}	2.24×10^{6}	4.14×10^{6}
n_0	1.14×10^{11}	2.73×10^{11}	4.37×10^{12}	7.64×10^{11}	5.17×10^{11}	2.33×10^{13}	3.31×10^{11}
M_C	0.065	0.118	0.989	1.089	0.887	0.547	0.339
M_N	2.72×10^{-8}	3.71×10^{-8}	4.45×10^{-6}	3.93×10^{-7}	3.93×10^{-7}	...	...
M_O	0.032	0.065	2.551	3.213	1.973	1.948	0.024
$M_{\rm Na}$	1.29×10^{-8}	1.74×10^{-8}	7.79×10^{-8}	3.70×10^{-8}	1.31×10^{-8}	1.31×10^{-8}	...
$M_{\rm Mg}$	1.81×10^{-5}	2.36×10^{-5}	8.84×10^{-4}	5.90×10^{-3}	3.26×10^{-3}	3.26×10^{-3}	...
$M_{\rm Al}$	1.91×10^{-8}	4.06×10^{-8}	5.89×10^{-8}	6.70×10^{-8}	2.17×10^{-8}	2.17×10^{-8}	...
$M_{\rm Si}$	1.26×10^{-6}	2.41×10^{-6}	1.42×10^{-5}	1.57×10^{-5}	5.19×10^{-6}	5.19×10^{-6}	...
$M_{\rm Ca}$	7.03×10^{-8}	1.28×10^{-7}	1.07×10^{-6}	1.18×10^{-6}	3.82×10^{-7}	3.82×10^{-7}	...
$M_{\rm Fe}$	8.62×10^{-7}	1.76×10^{-6}	1.47×10^{-5}	1.05×10^{-5}	4.7×10^{-6}	4.7×10^{-6}	...

Notes. Each model name identifies the progenitor mass; the additional labels—where present—1D or 3D specify the set of observed abundances used in model calibration (with default values being 3D, see text). The last two columns identify the two layers (A and B) of the unmixed ejecta of the 80 $M_\odot$-1D model.

Table 2

Masses of CO, SiO, O_2, C_2 Molecules in Faint SN Progenitor Ejecta and Masses of AC Grains ($M_\odot$)

	13 $M_\odot$	15 $M_\odot$	50 $M_\odot$	80 $M_\odot$	80 $M_\odot$	80 $M_\odot$	80 $M_\odot$
	3D	3D	3D	3D	1D	1D-A	1D-B
$M_{\rm CO}$	0.0246	0.074	2.29	2.15	1.44	1.276	0.043
$M_{\rm 2}$	2.91×10^{-8}	5.77×10^{-8}	6.21×10^{-5}	6.29×10^{-5}	2.42×10^{-5}	0.513	...
$M_{\rm C_2}$	–	–	–	–	–	...	0.21
$M_{\rm SiO}$	8.60×10^{-8}	2.73×10^{-7}	2.02×10^{-5}	1.49×10^{-5}	3.48×10^{-6}	8.11×10^{-6}	...
$M_{\rm AC}$	0.0544	0.0862	0.00557	0.165	0.269	—	0.112

Notes. Each model name identifies the progenitor mass; the additional labels—where present—1D or 3D specify the set of observed abundances used in model calibration (with default values being 3D, see text). The last two columns refer to the two layers (A and B) of the unmixed ejecta of the 80 $M_\odot$-1D model.

kinetic approach: in S. Marassi et al. (2014, in preparation) we have applied the model to a 15 $M_\odot$ Type IIP SN with solar metallicity and a stratified ejecta, and we find that the mass of CO at the onset of dust nucleation is in excellent agreement with results obtained by Sarangi & Cherchneff (2013) for the same SN progenitor.

We construct the ejecta models using as initial conditions the thermo-dynamical properties obtained by the SN explosion simulations (Limongi & Chieffi 2012). The ejecta follow an adiabatic expansion and the temperature evolution is given by

$$T = T_0 \left[1 + \frac{v_{\rm eje}}{R_0} t \right]^{3(1-\gamma)}, \qquad (1)$$

where $\gamma = 1.41$ is the adiabatic index, $v_{\rm eje}$ is the ejecta expansion velocity,

$$v_{\rm eje} = \sqrt{\frac{10 \, E_{\rm kin}}{3 \, M_{\rm eje}}}, \qquad (2)$$

and T_0 and R_0 are the temperature and radius of the He core at the initial time $t = t_0$ and are extracted from the simulation

outputs. The initial time t_0 is chosen to correspond to the time when the radius of the He core, $R_{\rm He_{core}}$, reaches a temperature of $T_0 = 10^4$ K. All these quantities and the initial gas number density $n_0(t = t_0)$ are shown in Table 1 for different SN progenitor models.

It is well known that the formation of CO molecules subtracts C-atoms, limiting the formation of carbon grains. In the C-rich and Fe-poor ejecta of faint SNe, the main molecular destruction process, collisions with energetic electrons produced by the radioactive decay of ^{56}Co, is strongly inhibited.

For all the faint SN models we have explored, the formation of CO is dominated by radiative association reaction (Dalgarno et al. 1990),

$$C + O \rightarrow CO + h\nu \qquad (3)$$
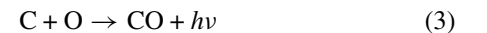
and by bimolecular, neutral-neutral reactions (UMIST database 2012)

$$C + O_2 \rightarrow CO + O \qquad O + C_2 \rightarrow CO + C \qquad (4)$$
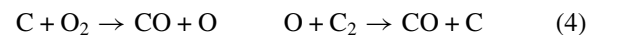
that involve O_2, C_2 molecules, and C, O atoms. As a result, the mass of CO that is formed ranges between 0.0544 $M_\odot$ and 0.269 $M_\odot$ (see Table 2). The formation of SiO in faint SN ejecta is strongly suppressed with respect to ordinary core-collapse

SNe, as a consequence of the very small initial abundance of Si (see Tables 1 and 2). Additional molecular species, such as O_2 and C_2, form through radiative association reactions (Andreazza & Singh 1997, Babb & Dalgarno 1995),

$$C + C \rightarrow C_2 + h\nu \quad O + O \rightarrow O_2 + h\nu \quad (5)$$
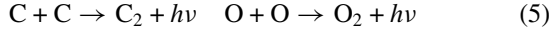
and through the inverse bimolecular process showed in Equation (4) in a non-negligible amount only if the ejecta is stratified (see Table 2).

Following Bianchi & Schneider (2007), our dust calculation is based on CNT. When a gas becomes supersaturated, particles (monomers) aggregate in a seed cluster that subsequently grows by the accretion of other monomers. The accretion process is regulated by the collision rate of the key species and depends on the sticking coefficient, defined as the probability that an atom colliding with a grain will stick to it. We show the results obtained assuming that the seed clusters are formed by a minimum of two monomers and that the sticking coefficient is equal to 1 for all grain species. The chemical composition and size at condensation and the basic data necessary for the dust formation calculations are shown in Table 2 of Nozawa & Kozasa (2003). The thermal and optical properties of the resulting dust materials can be found in Table A1 of Bianchi & Schneider (2007), to which we refer the interested reader. The nucleation process, together with accretion, results in typical log-normal grain size distributions (Todini & Ferrara 2001; Nozawa & Kozasa 2003).

If faint SN are believed to be powered by a spherical-like explosion, mixing occurs by means of Rayleigh–Taylor instabilities only in the innermost shells (Joggerst et al. 2009), up to a mass-coordinate that is very close to the mass-cut (M_{cut}). Hence the material beyond the mass cut is likely to be stratified and dust nucleation in unmixed ejecta provides a more realistic estimates of the total mass of dust produced. To enable a more direct comparison with previous results (Schneider et al. 2012b), where dust formation in uniformly mixed, Population III ordinary core-collapse SNe has been considered, we first present the results adopting uniformly mixed ejecta and then extend the calculation to stratified ejecta.

3.1. Dust Formation in Uniformly Mixed Ejecta

Contrary to ordinary core collapse SNe (Schneider et al. 2012b), the only grain species that form in non-negligible amounts in faint SNe is amorphous carbon (AC). This is due to the peculiar metal composition of faint SN ejecta, that are dominated by C-atoms and where the abundances of Mg, Si, Al, and Fe are too small to enable the formation of silicates, magnetite, or alumina grains. In Table 2 we show the resulting masses of molecules and of AC grains for all the explored faint SN models. We show that the mass of dust increases with the mass of the SN progenitor, ranging from $M_{dust} = 5.4 \times 10^{-2}\, M_\odot$ for the 13 $M_\odot$ model to $M_{dust} = 0.269\,(0.165)\, M_\odot$ for the 80 $M_\odot$-1D (3D) model, consistent with the larger metal mass initially present in the ejecta. The only exception is represented by the 50 $M_\odot$ model, which produces the smallest mass of dust, $M_{dust} = 5.6 \times 10^{-3}\, M_\odot$. The reason for this behavior resides in the larger mean ejecta density of the 50 $M_\odot$ model, which increases the rates of the major processes leading to the formation of CO molecules. This can be understood by looking at Figure 2 where we show the time evolution of temperature, density, CO, and AC masses for the 50 $M_\odot$, and the 80 $M_\odot$ models. In the 50 $M_\odot$ SN model, dust nucleation starts when

the temperature has dropped below the AC grain condensation temperature, ~1940 K, roughly 60 days after the explosion, when the number density is $n_0 = 2.58 \times 10^{10}\, cm^{-3}$. Conversely, in the 80 $M_\odot$ SN model, the gas temperature drops to ~2000 K only 86 days after the explosion, when the number density is $n_0 = 7.15 \times 10^9\, cm^{-3}$. Comparing the chemical reaction rates to the expansion rate, k_{dyn}, defined as

$$k_{dyn} = 1/t = \frac{v_{eje}}{R(t)}, \quad (6)$$

where v_{eje} is the ejecta velocity and $R(t)$ is the ejecta position at a given time t after explosion, we can determine $t = t_{fo}$, the time at which each reaction rate becomes longer than the expansion rate, leading to a "freeze-out" of the corresponding chemical species (Cherchneff & Dwek 2009). The mass of CO molecules at t_{fo} and at the onset of dust nucleation (t_{nucl}) largely determines the resulting dust mass. For the 50 $M_\odot$ model, we find that $M_{CO}(t_{fo}) = 2.21\, M_\odot$ and, at this stage, the carbon mass locked in CO molecules is $0.945\, M_\odot$. When nucleation starts, $M_{CO}(t_{nucl}) = 2.29\, M_\odot$ and $0.982\, M_\odot$ mass of carbon is locked in CO molecules. Hence, out of the $0.988\, M_\odot$ of C atoms initially present in the ejecta (see Table 1), only ~$6 \times 10^{-3}\, M_\odot$ are available to form C-grains. If we do the same calculation for the 80 $M_\odot$-3D model, we find $M_{CO}(t_{fo}) = 1.258\, M_\odot$, $M_{CO}(t_{nucl}) = 1.438\, M_\odot$, and the mass of carbon atoms locked in CO at nucleation is $0.616\, M_\odot$, so that there are still $0.27\, M_\odot$ of carbon free to form C-grains. Hence, the reason why the 50 $M_\odot$ model forms the least amount of dust is the higher efficiency of CO formation, which leads to a carbon depletion in CO molecules of 95% at freeze-out. Note that in less massive progenitor models, the ejecta composition is characterized by an initial mass of C greater than the O mass (see Table 1); this contributes to decreased C depletion in CO molecules, increasing the resulting mass of AC grains.

3.2. Dust Formation in Unmixed Ejecta

Recently, Joggerst et al. (2009) have pointed out that zero metallicity SN progenitors experience more fallback and a smaller degree of mixing, induced by Rayleigh–Taylor instabilities, than their solar metallicity counterparts. As a result, we expect that the ejecta of faint SNe are likely to be unmixed. Hence, it is important to explore how the mass of dust estimated above depends on the adopted mixing efficiency. We consider a 80 $M_\odot$-1D SN progenitor model. The stratified ejecta consists of two layers, which differ mainly for the different abundance of carbon and oxygen: the inner one (layer A) is characterized C/O < 1 whereas in the outer one (layer B) C/O > 1 (see Table 1). In Figure 3, we show the time evolution of the temperature, density, AC, and molecular masses formed in the two layers A and B. In the inner layer A, all the carbon is rapidly locked in CO molecules and consequently C-grains do not form. The oxygen is first depleted in CO molecules and then in O_2 molecules. Conversely, in the outer layer B, only ~5% of carbon is locked in CO, ~26% of carbon is locked in C_2, and the remaining C atoms are free to form $0.112\, M_\odot$ of AC grains as shown in the right bottom panel in Figure 3. O_2 and C_2 form mainly due to radiative association processes. Note that in the present formalism, there is no connection between the formation of C2 and the formation of carbon dust; however, if all the C2 were to transform into carbon dust, the final AC mass would amount to ~$0.2\, M_\odot$. In the stratified ejecta, due to the different temperature evolution of the two layers, CO molecules start to
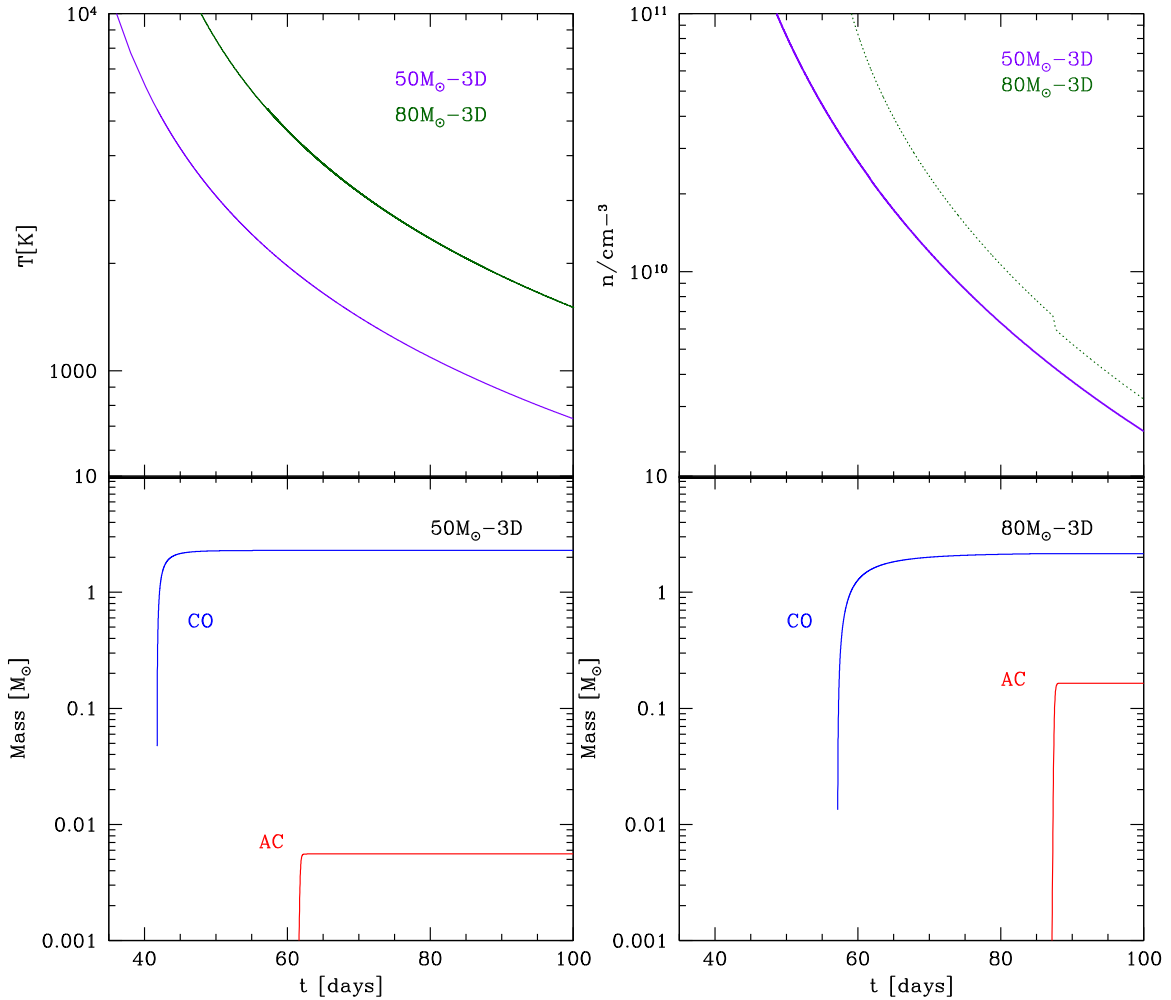
Figure 2. Upper panels: temperature and density evolution for 50 $M_\odot$ and 80 $M_\odot$ 3D mixed models. Bottom panels: time evolution of CO molecule and dust for 50 $M_\odot$ and 80 $M_\odot$ 3D mixed models.

(A color version of this figure is available in the online journal.)

form at an earlier time than in the corresponding mixed model, and the resulting dust mass is ∼40% smaller.

3.3. Dust Destruction by the Reverse Shock

As the ejecta expand, a forward shock is driven into the ISM, which compresses and heats the ambient gas. The shocked ambient gas drives a reverse shock in the ejecta, which in ∼10^3 years has swept over a considerable fraction of its volume. The passage of the reverse shock can be particularly destructive for the small dust grains, due to the transfer of thermal and kinetic energy during impact with gas particles (sputtering). We estimate the mass of newly formed dust that is able to survive the passage of the reverse shock and enrich the ISM following the same model developed by Bianchi & Schneider (2007).

The dynamics of the reverse shock is described using the analytical approximations of Truelove & McKee (1999) for a uniform density distribution inside the ejecta, which allow us to compute the velocity of the shock as a function of the SN explosion energy, E_{kin}, the mass of the ejecta, M_{eje}, and the density of the ISM, ρ_{ISM}. For each SN model, we compute the dynamics of the reverse shock using the same values for E_{kin} and M_{eje} that have been used in the dust formation calculations (see Table 1). In addition, we study the effect of three different ISM environments, with $\rho_{ISM} = 10^{-25}, 10^{-24}$ and 10^{-23} g cm^{-3}.

We assume that dust grains are distributed uniformly within the ejecta, and that the size distribution is the same everywhere. In Figure 4 we show the grain size distribution that results from grain condensation and accretion in the (fully mixed) ejecta of the 50 $M_\odot$ and 80 $M_\odot$ SN models. Initially, the grain sizes follow a log-normal distribution in the range $(10^{-2}$–$0.5)\,\mu$m. However, in the shells that have been visited by the reverse shock, dust grains are bathed in a gas heated to high temperature (of the order of 10^7–10^8 K). In addition, the gas is slowed down, decoupled from the grains and transfer thermal and kinetic energy to the grains by means of collisions. Following Bianchi & Schneider (2007), we consider both thermal and non-thermal sputtering. Note that since the reverse shock velocity, which is of the order of 10^3 km s^{-1}, is larger when the SN explodes in a denser circumstellar medium (Truelove & McKee 1999), the reverse shock travels faster inside the ejecta and encounters a gas at higher density. This increases the effect of sputtering. The effects of the reverse shock on the grain size distribution function is also shown in Figure 4: the larger grains are eroded and this produces a shift of the distribution to lower grain sizes, with a tail extending to a few Å. Note that when the number of monomers in each grain becomes less than 2, the grain is evaporated, returning the metals into the gas phase (see Equation (2) in Bianchi & Schneider 2007).
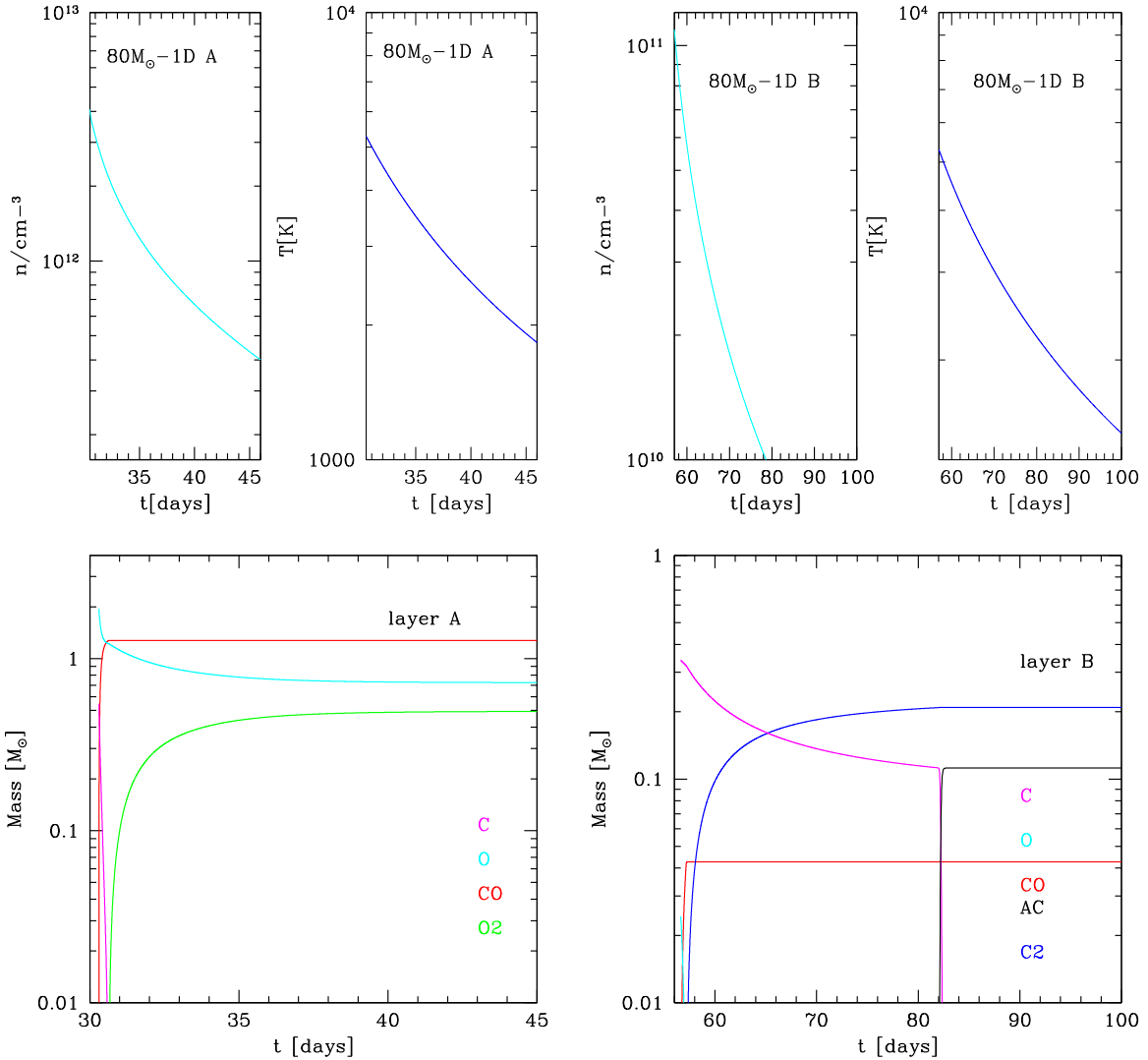
Figure 3. Upper panels: temperature and density evolution for the stratified 80 $M_\odot$-1D (left panels, layer A; right panels, layer B). Bottom panels: time evolution of the mass in dominant molecular species, and carbon and oxygen in layer A (left panel) and in layer B (right panel).

(A color version of this figure is available in the online journal.)

The destructive efficiency of the reverse shock is shown in Figure 5, where we plot the mass of dust that survives for increasing shock strengths. Depending on the progenitor model, the fraction of newly formed dust that is able to survive ranges between 80% to a few percent. These numbers are in agreement with what has been found by other studies using hydrodynamical simulations (Nozawa et al. 2007; Silvia et al. 2010, 2012). In particular, by post-processing an idealized numerical simulation of a planar shock wave impacting a dense, spherical clump, Silvia et al. (2010, 2012) have calculated grain sputtering for a variety of species and size distributions. By altering the clump overdensity and the shock velocity, they find that grains with radii smaller than 0.1 μm are sputtered to much smaller radii and often completely destroyed, and that the percentage of dust mass that survives critically depends on the initial grain size distribution and on the velocity of the reverse shock, ranging between complete destruction to $\sim$44% survival for the largest and most robust grains.

Given that the dust produced in faint SN ejecta is composed only by AC grains, the fraction of mass that gets destroyed is returned into the gas phase under the form of C atoms. The resulting carbon condensation efficiencies, defined as the ratio

of the mass of AC grains relative to the initial mass of C atoms present in faint SN ejecta are shown in Table 3. These, together with the gas-phase abundances of the other elements present in the ejecta represent the initial conditions for the collapse calculations described in the next section.

4. THE STAR FORMING ENVIRONMENT OF SMSS J031300

In this section, we test the hypothesis that SMSS J031300 has formed out of the collapse and fragmentation of a gas cloud that has been pre-enriched by the ejecta of one of the Population III faint SNe studied in the previous section. We first discuss the expansion of the ejecta into the surrounding ISM and then the subsequent recollapse of the star forming cloud, to assess the relative role of fine-structure line and dust cooling for the formation of SMSS J031300.

4.1. Ejecta Expansion and Mixing with the ISM

The mixing and fallback model—as first introduced by Umeda & Nomoto (2002)—naturally predicts a stratified ejecta: the inner material is assumed to be mixed by the growth of

Table 3
Properties of Models that we Investigate with the Critical Abundances of Carbon, [C/H]$_{cr}$, for Low-mass Star Formation

SN Progenitor	Model	$f^{ini}_{C,cond}$	$\mathcal{D}_{ini}$	$D_{trans,ini}$	r^{cool}_C (μm)	$f^*_{C,cond}$	(C/H)$_{cr}$
13 $M_\odot$	norev	0.84	9.10×10^{-6}	-4.07	0.108	0.84	-4.65
	rev1	0.53	5.77×10^{-6}	-3.07	0.104	0.63	-4.54
	rev2	0.26	2.83×10^{-6}	-2.82	0.119	0.63	-4.48
	rev3	0.10	1.05×10^{-6}	-2.71	0.148	0.63	-4.39
15 $M_\odot$	norev	0.73	7.90×10^{-6}	-4.23	0.177	0.73	-4.37
	rev1	0.53	5.78×10^{-6}	-3.26	0.170	0.59	-4.30
	rev2	0.29	3.16×10^{-6}	-2.94	0.191	0.59	-4.25
	rev3	0.12	1.32×10^{-6}	-2.80	0.228	0.59	-4.17
50 $M_\odot$	norev	0.0056	6.10×10^{-8}	-3.41	0.014	0.0059	-3.38
	rev1	0.0013	1.38×10^{-8}	-3.40	0.012	0.0013	-2.79
	rev2	0.0004	$\mathbf{4.26 \times 10^{-9}}$	-3.40	0.012	0.0004	$\mathbf{-2.30}$
	rev3	0.0001	$\mathbf{1.30 \times 10^{-9}}$	-3.39	0.012	0.0001	$\mathbf{-1.77}$
80 $M_\odot$-3D	norev	0.15	1.64×10^{-6}	-3.25	0.073	0.15	-4.07
	rev1	0.08	8.07×10^{-7}	-3.12	0.067	0.08	-3.80
	rev2	0.03	3.69×10^{-7}	-3.07	0.064	0.03	-3.49
	rev3	0.01	1.17×10^{-7}	-3.04	0.061	0.01	-3.01

Notes. We here show our models with metal abundances fitted for 3D stellar atmospheric models by Keller et al. (2014). r^{cool}_C and $f^*_{C,cond}$ are, respectively, the characteristic radii of carbon grains (see text) and the carbon condensation efficiency at density $n_H = 10^{12}$ cm^{-3}, resulting from our collapse calculations with the effects of grain growth. Carbon abundance is set to the observed value, [C/H] = -2.60. The values in bold face are below the corresponding critical limits, $D_{trans} > -3.5 \pm 0.2$ and $\mathcal{D}_{cr} = [2.6\text{–}6.3] \times 10^{-9}$.
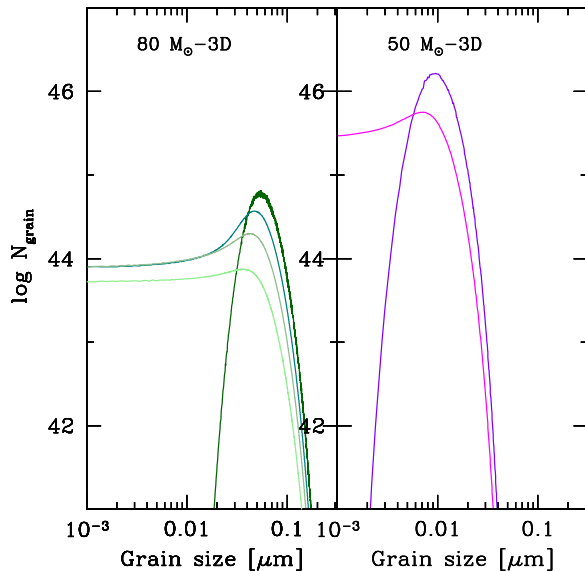

Figure 4. Size distribution for grains formed in the ejecta of 80 $M_\odot$-3D and 50 $M_\odot$-3D models, for no reverse shock model (norev) and for models with a circumstellar medium density of $\rho_{ISM} = 10^{-25}$ (rev1), 10^{-24} (*rev* 2) and 10^{-23} g cm^{-3} (*rev* 3), from top to bottom. For the 50 $M_\odot$ model, the rev2 and rev3 cases are out of scale.

(A color version of this figure is available in the online journal.)

Figure 5. Histograms showing the mass of dust at the end of nucleation, and after the passage of a reverse shock of increasing intensity for all the faint SN progenitors considered in the present study. From top to bottom: no reverse shock models (norev), models with a circumstellar medium density of $\rho_{ISM} = 10^{-25}$ (rev1), 10^{-24} (rev2), and 10^{-23} g cm^{-3} (rev3). For the 50 $M_\odot$ model the rev2 and rev3 cases are out of scale.

(A color version of this figure is available in the online journal.)

Rayleigh–Taylor instabilities during shock propagation, while the ejecta is dominated by the external material plus a small fraction of the mixed gas near the mass-cut. The mixing efficiency is still a matter of debate due to the complexity of the mixing/fallback scenario, which depends on the explosion energy, the gravitational potential, and the asphericity during the collapse. This is the reason why we have studied dust formation in both perfectly mixed and stratified ejecta. Yet, when we compare the observed surface elemental abundance of a stellar fossil, such as SMSS J031300, with the yields of a single Population III SN, we make t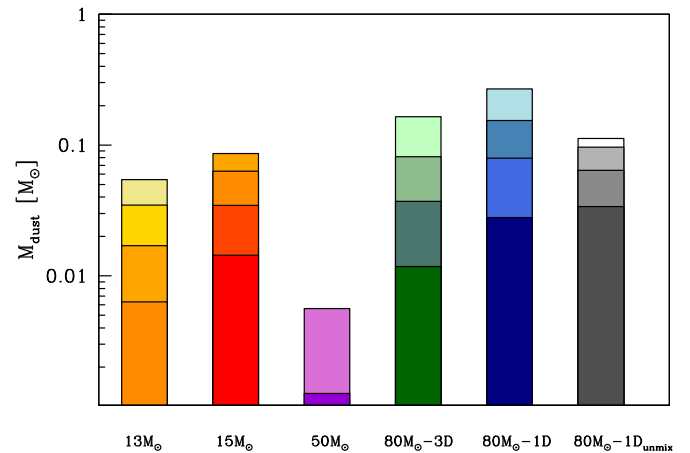he implicit assumption that the ejecta material has uniformly enriched the parent star-forming cloud. Hence, whatever the degree of mixing at nucleation, 45–80 days after the explosion, or after the passage of the reverse shock, $(2.6\text{–}3.4) \times 10^3$ years later, the ejecta material needs to be perfectly mixed into the star forming cloud before its subsequent collapse.

An estimate of the maximum timescale available to fully mix the enriched material can be obtained by computing the total mass and radius of the cloud, M_{cloud}, in which the ejecta needs to be diluted in order to match the observed metallicity on the surface of SMSS J031300, $Z_{obs} \sim 2.67 \times 10^{-3} Z_\odot$ (Keller et al. 2014),

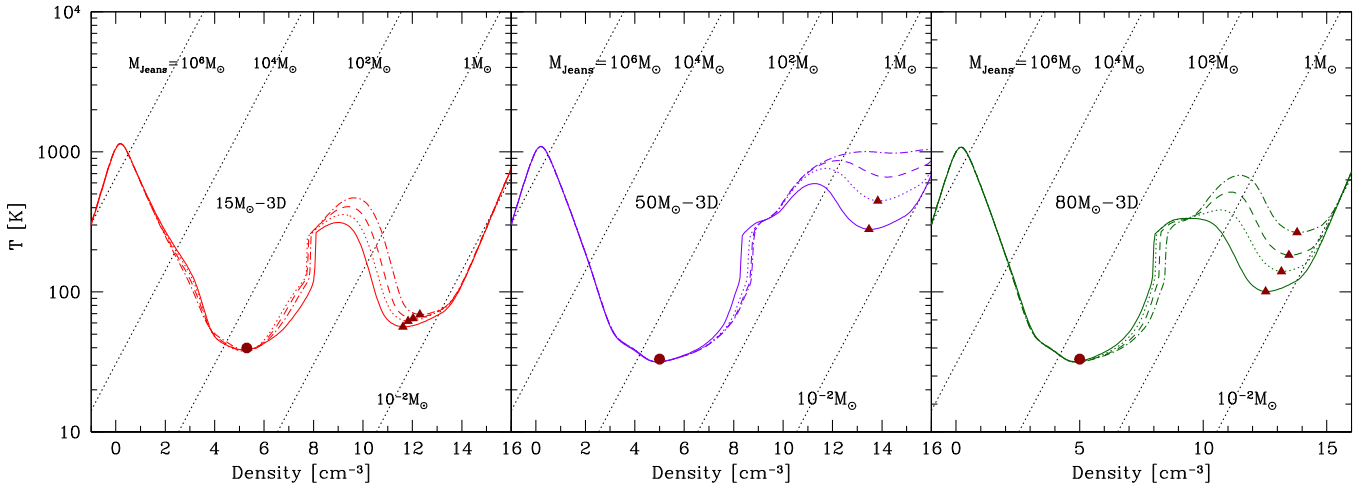$$M_{cloud} = \frac{M_{met,ejecta}}{Z_{obs} X_H}, \qquad (7)$$

Figure 6. Temperature evolution as a function of the central density of clouds pre-enriched by Population III faint SN explosions of 15 $M_\odot$ (left), 50 $M_\odot$ (middle), and 80 $M_\odot$-3D (right) stars. Solid curves represent models with no reverse shock, dotted-, dashed- and dot-dashed curves represent models with a circumstellar medium density of $\rho_{ISM} = 10^{-25}, 10^{-24}$ and 10^{-23} g cm^{-3}, hence an increasing reverse shock destructive efficiency. Red triangles mark the states where gas fragmentation conditions are met.

(A color version of this figure is available in the online journal.)

where $X_H = 0.75$ and we have assumed an ISM with primordial composition. We find that M_{cloud} is an increasing function of the progenitor mass, since more massive progenitors have larger metal yields, and ranges between 10^4 and $2 \times 10^5 \, M_\odot$. This gas mass is roughly consistent with the baryonic content of a $\sim 10^6 \, M_\odot$ mini-halo. The radius of the cloud depends on the density of the ISM (ρ_{ISM}): to be consistent with the reverse shock models described in the previous section, we assume values in the range $[10^{-26} – 10^{-23}]$ g cm^{-3}, where the lower limit approximately corresponds to the critical density at $z = 10$. The corresponding cloud radius is

$$R_{cloud} = \left[\frac{3 M_{cloud}}{4\pi \rho_{ISM}} \right]^{1/3} \qquad (8)$$

and varies in the range $20 \, pc \leqslant R_{cloud} \leqslant 100 \, pc$, which is reached by the SN shock in its Sedov–Taylor phase on a timescale $t_{exp} = R_{cloud}^{5/2} (\rho_{ISM}/E_{exp})^{1/2} \sim 0.2$–$10$ Myr.

Following Madau et al. (2001), we can estimate the growth timescale of Rayleigh–Taylor instabilities as $t_{RT} \approx (l_s/2\pi g)^{1/2}$, where g is the gravitational acceleration and l_s is the spatial scale to be mixed. Using the values computed above for the cloud mass and radius, we find $t_{RT} = 0.4$–3 Myr, depending on the ISM density. Hence, in less than a few megayears after the explosion of a faint Population III SN, the ejecta material may have already mixed and enriched the gas out of which second generation stars form. The resulting stellar mass depends on the cooling and fragmentation properties of the collapsing gas, which we investigate in the following section.

4.2. Cooling and Fragmentation of the Collapsing Cloud

We perform a one-zone semi-analytic collapse calculation to follow the temperature evolution of the cloud (Omukai 2000, Omukai et al. 2005), setting the abundances of heavy elements and dust species as inferred from the SN dust models described in the previous section. We refer the interested reader to Chiaki et al. (2014) for a detailed description of the model.

In this collapse calculation, we solve non-equilibrium chemistry of 27 gas-phase species (H$^+$, e^-, H, H$^-$, H$_2$, D$^+$, D, HD, C$^+$, C, CH, CH$_2$, CO$^+$, CO, CO$_2$, O$^+$, O, OH$^+$, OH, H$_2$O$^+$, H$_2$O,

H$_3$O$^+$, O$_2^+$, O$_2$, Si, SiO, and SiO$_2$) with a chemical network of 55 reactions. Radiative cooling owing to atoms/ions (C I, C II, and O I) and molecules (H$_2$, HD, CO, OH, and H$_2$O), and the heating/cooling by H$_2$ formation/destruction are computed self-consistently at each time. Gas cooling by heat transfer between gas and dust is calculated as the sum over all dust species and size bins. In addition to the dust mass that is present in the gas cloud at the onset of collapse, we also treat accretion of gas-phase metal species onto dust grains during the collapse (grain growth, Nozawa et al. 2012; Chiaki et al. 2014). For the purpose of the present analysis, we set the cosmic microwave background (CMB) temperature at $T_{CMB} = 27.3$ K, corresponding to $(1 + z) = 10$ (see Schneider & Omukai 2010 for the effects of the CMB temperature floor on the collapse of clouds at different metallicities).

Figure 6 shows the cloud evolution in the temperature–density plane. Each panel represents the results assuming that the cloud has been pre-enriched by the explosion of an individual Population III faint SN model. We have selected the results of three different progenitor masses (the 13 and 15 $M_\odot$ models lead to very similar results) adopting dust yields formed in uniformly mixed ejecta (3D models, although the results are not affected by the set of reference abundances adopted in the explosion calibration). For each of these, we consider the decreasing dust-to-metal ratios that emerge from the passage of the reverse shock of increasing intensity. The initial dust-to-gas mass ratio at the onset of collapse, $\mathcal{D}_{ini}$ and initial transition discriminant $D_{trans,ini}$ are shown in Table 3, where we have written in bold only the values that are below the corresponding critical limits. Hence, we would expect metal-line cooling to be effective for all but models 13 and 15 $M_\odot$ in the no reverse shock case, and dust cooling to be effective for all but models 50 $M_\odot$ in the two stronger reverse shock cases (rev2 and rev3).

We can compare these simple expectations with full collapse calculations. The circles and triangles in the figure mark the states where fragmentation conditions are met (Schneider et al. 2010). At densities $n_H \sim 10^5$ cm^{-3}, fragmentation is due to line-cooling. In the 13 and 15 $M_\odot$ models, the dominant coolants are HD and C I. For models with moderate reverse shock destruction (norev, rev1), $f_{C,cond}^{ini} > 0.5$ and—as a result—H$_2$ formation on grain surface is very efficient, enabling the formation

of HD molecules. On the other hand, C I cooling efficiency is comparable to (3D cases) or exceeds (1D cases, where [C/H] is larger than 3D) HD cooling for rev2 and rev3 models.[8] For the larger progenitor mass models (50 and 80 $M_\odot$), the dominant coolant at intermediate densities is C I as a result of the lower initial condensation efficiencies. Yet, as shown by the diagonal lines in the three panels, the characteristic masses of the fragments formed in this early stage of collapse (the Jeans mass at the density where instability occurs) are estimated to be $\sim 100\ M_\odot$.

It is important to note that although sputtering of AC grains releases C atoms in the gas phase that may be potentially accreted onto the surviving grains at a later stage of the collapse, grain growth has a non-negligible impact on the results only if C/O $>$ 1 at the onset of collapse. In fact, AC grain growth is prevented by efficient formation of CO molecules at $n_H \sim 10^4$ cm^{-3} (Chiaki et al. 2014). This is confirmed by comparing the carbon condensation efficiencies at the onset of collapse, $f^{ini}_{C,cond}$, and a later stage of the collapse, $f^*_{C,cond}$, when the density is large enough for grain growth to occur efficiently ($n_H = 10^{12}$ cm^{-3}, see below). The values predicted by each model are shown in Table 3; as expected, grain growth has a non-negligible effect only for the 13 and 15 $M_\odot$ models with reverse shock. Hence, for all but the smallest progenitor mass models, the conditions for dust cooling and fragmentation are largely determined by the dust-to-gas ratio initially present in the cloud as a result of the SN explosion and the associated reverse shock.

Figure 6 shows that dust cooling is efficient at high densities $n_H = 10^{10}$–10^{14} cm^{-3} triggering fragmentation and potentially leading to the formation of a low-mass star such as SMSS J031300. The only two unsuccessful cases are associated with the 50 $M_\odot$ faint SN explosion with the stronger reverse shock models. Not surprisingly, in these two models the amount of dust that survives the passage of the reverse shock is not enough to keep the initial dust-to-gas mass ratio above the critical one, $\mathcal{D}_{cr} = [2.6\text{--}6.3] \times 10^{-9}$ (see Table 3).

Finally, it can be shown that the full collapse calculations confirm that even in unmixed models, which are characterized by smaller dust yields, dust-driven fragmentation conditions are met for all reverse shock cases considered, consistent with the fact that the initial dust-gas ratios are super-critical, varying in the range $\mathcal{D} = 7.94 \times 10^{-8}$–$1.11 \times 10^{-6}$.

Following Chiaki et al. (2014), we can estimate the critical elemental abundances that enable dust-induced fragmentation. For CEMP stars enriched by faint Population III SN explosions, carbon grains are the dominant species in the parent cloud; therefore, the critical dust-to-gas ratio can be easily associated with a critical carbon abundance,

$$A_{C,cr} = 1.4 \times 10^{-3} \frac{4\, s_C\, r_C^{cool}}{3 X f_{C,cond}(t)\, \mu_C}$$
$$\times \left(\frac{T}{10^3\ \mathrm{K}}\right)^{-1/2} \left(\frac{n_H}{10^{12}\ \mathrm{cm}^{-3}}\right)^{-1/2},$$

where s_C is the material density of carbon grains ($s_C = 2.28$ g cm^{-3}) and $r_C^{cool} = \langle r^3 \rangle_C / \langle r^2 \rangle_C$ is the characteristic grain radius for gas cooling (Chiaki et al. 2014). Table 3 shows the

cooling radii and the critical carbon abundances normalized to the solar value ($A_{C,\odot} = 2.69 \times 10^{-4}$ taken from the photospheric value in Asplund et al. 2009). Since the observed carbon abundance of SMSS J031300 is [C/H] $= -2.60$ (Keller et al. 2014). the critical conditions are satisfied by all the models but the 50 $M_\odot$ rev2 and rev3. This is consistent with the full collapse calculations. Hence we conclude that the formation of the CEMP star SMSS J031300, even with the lowest iron content currently observed, may have been triggered by dust cooling and fragmentation.

5. DISCUSSION AND CONCLUSIONS

The results presented in the previous section have been obtained using the dust and metal yields predicted for faint Population III SN explosions tailored to reproduce the observed elemental abundances of SMSS J031300. For the first time, we have studied the process of dust formation in carbon-rich, iron-poor ejecta that characterize these explosions. We find that carbon can be significantly depleted onto AC grains, with condensation efficiencies that can be as large as 75%. Due to the small abundance of other refractory elements in the ejecta, silicates, alumina, or magnetite grains do not form in the ejecta of faint Population III SNe. For most of the models we have explored, when normalized to the observed [C/H] that characterizes CEMP stars, the predicted dust-to-gas ratios in the parent star-forming cloud are large enough to trigger dust cooling and fragmentation, even without the contribution of grain growth.

If these results can be considered as representative for the general class of CEMP-no stars, which represent 90% of CEMPs with [Fe/H] < -3, then our study suggests that dust cooling and fragmentation may have been responsible for the formation of these low-mass stars.

In a recent work, Ji et al. (2014) have suggested that the early formation of low-mass stars may follow two potential pathways: in the dynamic pathway, many sub-clumps are formed through fine-structure line cooling. Dynamical interactions can lead to the ejection of a protostar from the parent cloud, so that a low-mass star can form even in the absence of dust cooling. In the thermal pathway, fragmentation due to fine-structure cooling is inhibited by the small abundance of gas-phase elements, and the entire cloud collapses. A high-density protostellar disk is formed at the center of the cloud, which then fragments and forms low-mass stars due to dust-cooling. Observational evidence for these two alternative pathways comes from the distribution of a sample of metal-poor halo stars and dwarf galaxy stars with [Fe/H] < -3.5 in a plane where the transition discriminant for line-cooling, D_{trans}, is on the y-axis and the [Si/H] (see their Figure 6) is on the x-axis; the latter quantity is used as an indication of the dust-to-gas ratio in the parent cloud, assuming that the dust is mostly made of silicates. When compared with the critical values for fine-structure-line and dust cooling, they find that stars that have an [Si/H] too low to form through silicon-based dust cooling are characterized by a large transition discriminant, and satisfy the criterion for fine-structure-line cooling and vice versa.

Our study questions this interpretation as it shows that CEMP stars form in C-rich gas, where silicates do not form and carbon dust is the dominant dust species. Hence, for CEMP stars, [C/H] is a better proxy for dust cooling than [Si/H]. In addition, we also show that fine-structure-line and dust cooling are not mutually exclusive: the collapsing gas cloud undergoes two distinct phases of fragmentation, one driven by line cooling
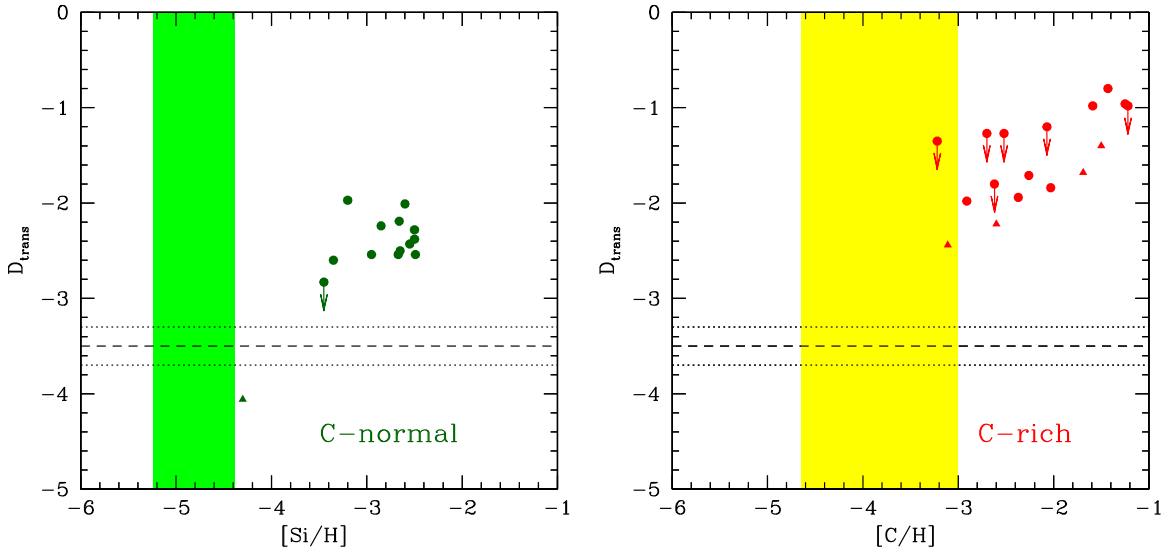
---

[8]　In our calculations, gas cooling is dominated by C I because we are neglecting the presence of a far-UV (FUV) radiation field. If some FUV is present, C I is photo-ionized and—as a result—C II dominates cooling. However, this does not affect our conclusions as the two cooling rates are similar.

Figure 7. Conditions for the formation of low-mass C-normal (left panel) and C-rich stars (right panel). Observations are taken from [Fe/H] < -3 sample of Norris et al. (2013). Points with triangles indicate the sub-sample of the five ultra-iron poor stars, with [Fe/H] < -4 currently known. The horizontal lines indicate the critical transition discriminant $D_{\rm trans,cr} = -3.5 \pm 0.2$ for fine-structure-line cooling (Frebel & Norris 2013). The vertical shaded regions indicate the range of critical Si (left panel) and C (right panel) abundances that would enable Si-dominated dust and C-dominated dust to activate dust cooling (see text). The arrows indicate stars where either the C or the O abundances was not measured and only an upper limit was available.

(A color version of this figure is available in the online journal.)

(either by metal lines, such as C I, C II or by molecular transitions of H_2 and HD) at $n_H \sim 10^4$ cm^{-3}, which leads to the formation of $\sim 100\, M_\odot$ sub-clumps; and the other, driven by dust cooling at $n_H = 10^{10}$–10^{14} cm^{-3}, which triggers the formation of low-mass stars (see also Tanaka & Omukai 2014). Thus, the thermal pathway may be responsible for the formation of both C-rich and C-normal stars, even at the lowest [Fe/H] currently observed, although the dynamic pathway may operate as well.

Unfortunately, it is not straightforward to estimate the dust-to-gas ratio of the parent gas cloud from the observed elemental abundances, similar to what is done for the transition discriminant. In fact, the dust properties (its composition and size distribution) depend on the nature of the SN explosions that have dominated the early enrichment and on the level of destruction suffered by the newly formed dust by the passage of the reverse shock, although the latter process may be mitigated by grain growth during the collapse. Using the results that we have obtained in the present study as a proxy for the general class of C-rich metal-poor stars and the results obtained by Schneider et al. (2012b) and Chiaki et al. (2014) for the star SDSS J1029151 as a proxy for the general class of C-normal metal-poor stars, we can draw the following guidelines: for C-rich stars, carbon condensation efficiencies into dust of 0.01–0.84 translate into critical carbon abundances of $-4.65 < \text{[C/H]}_{\rm cr} < -3.01$; for C-normal stars, the dominant dust compounds are forsterite (Mg_2SiO_4) and enstatite ($MgSiO_3$), with Mg and Si condensation efficiencies which range between 0.2 and 0.6 and associated critical abundances of $-5.02 < \text{[Mg/H]}_{\rm cr} < -4.73$ and $-5.24 < \text{[Si/H]}_{\rm cr} < -4.73$ (see Table 1 in Chiaki et al. 2014).

In Figures 6 and 7, we compare these predictions with observational data taken from the sample of C-normal and C-rich stars with [Fe/H] < -3 investigated by Norris et al. (2013). As shown in Caffau et al. (2011), SDSS J1029151 is the only star, discovered until now, that falls in the forbidden zone for fine-structure line cooling (indicated by the triangle below $\mathcal{D}_{\rm cr}$ in Figures 7 and 8) and no stars appear to fall in the forbidden zone for dust cooling, although there are two C-rich stars, HE0557-
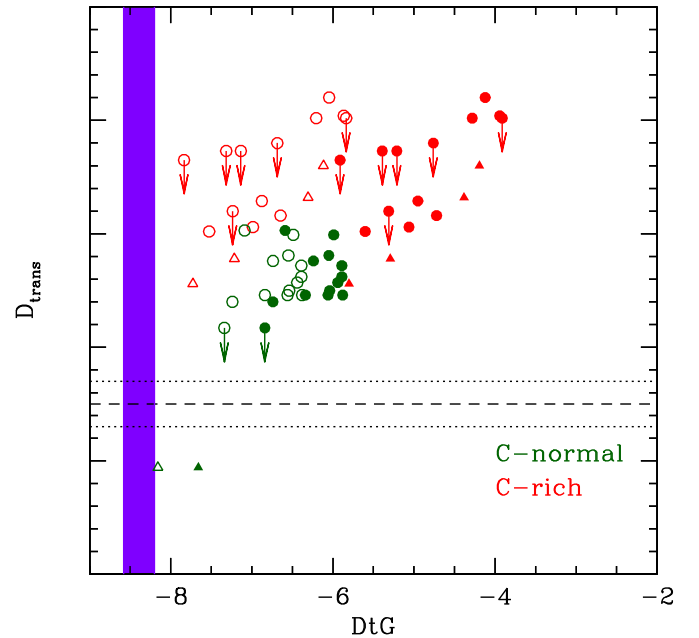

Figure 8. Same as in Figure 6 but the data are not plotted as a function of the estimated dust-to-gas mass ratio; for each star we show two values of the dust-to-gas mass ratio, obtained using the maximum (filled data points) and minimum (empty data points) condensation efficiencies for C (C-rich) and Si (C-normal) stars (see text). The vertical shaded region represent the critical dust-to-gas ratio of $\mathcal{D}_{\rm cr} = [2.6$–$6.3] \times 10^{-9}$ for dust-cooling (Schneider et al. 2012a).

(A color version of this figure is available in the online journal.)

4840 (Norris et al. 2007) and HE0057-5959 (Yong et al. 2013b), which appear to be close to the critical range.

If we represent the critical conditions in terms of the dust-to-gas ratio, as in Figure 8, we see that C-normal and C-rich stars do not appear to follow different distributions on the plane, although—as expected—the C-normal stars have systematically lower $D_{\rm trans}$ and lower dust-to-gas-ratios, $\mathcal{D}$.

More importantly, the two criteria for low-mass star formation do not appear to be mutually exclusive, but rather point to a single pathway for the formation of the first low-mass stars in the universe.

REFERENCES

Andreazza, C. M., & Singh, P. D. 1997, MNRAS, 287, 287
Aoki, W., Beers, T. C., Honda, S., & Carollo, D. 2010, ApJL, 723, L201
Asplund, M., Grevesse, N., Sauval, A. J., & Scott, P. 2009, ARA&A, 47, 481
Babb, J. F., & Dalgarno, A. 1995, PhRvA, 51, 3021
Beers, T. C., & Christlieb, N. 2005, ARA&A, 43, 531
Bianchi, S., & Schneider, R. 2007, MNRAS, 378, 973
Bromm, V., & Loeb, A. 2003, Natur, 425, 812
Caffau, E., Bonifacio, P., Francois, P., et al. 2011, Natur, 477, 67
Campbell, S. W., Lugaro, M., & Karakas, A. I. 2010, A&A, 522, L6
Cayrel, R., Depagne, E., Spite, M., et al. 2004, A&A, 416, 1117
Cherchneff, I., & Dwek, E. 2009, ApJ, 703, 642
Cherchneff, I., & Dwek, E. 2010, ApJ, 713, 1
Chiaki, G., Nozawa, T., & Yoshida, N. 2013, ApJL, 765, L3
Chiaki, G., Schneider, R., Nozawa, T., et al. 2014, MNRAS, 439, 3121
Dalgarno, A., Du, M. L., & You, J. H. 1990, ApJ, 349, 675
Donn, B., & Nuth, J. A. 1985, ApJ, 288, 187
Frebel, A., Johnson, J. L., & Bromm, V. 2007, MNRAS, 380, L40
Frebel, A., & Norris, J. E. 2013, in Planets, Stars and Stellar Systems, ed. T. D. Oswalt & G. Gilmore (Dordrecht: Springer), 55
Heger, A., & Woosley, S. E. 2010, ApJ, 724, 341
Hirano, S., Hosokawa, T., Yoshida, N., et al. 2014, ApJ, 781, 60
Hirschi, R. 2007, A&A, 461, 571
Ji, A. P., Frebel, A., & Bromm, V. 2014, ApJ, 782, 95
Joggerst, C. C., Woosley, S. E., & Heger, A. 2009, ApJ, 693, 1780

Keller, S. C., Bessel, M. S., Frebel, A., et al. 2014, Natur, 506, 463
Limongi, M., & Chieffi, A. 2003, ApJ, 592, 404
Limongi, M., & Chieffi, A. 2006, ApJ, 647, 483
Limongi, M., & Chieffi, A. 2012, ApJS, 199, 38L
Lucatello, S., Tsangarides, S., Beers, T. C., et al. 2005, ApJ, 625, 825
Madau, P., Ferrara, A., & Rees, M. J. 2001, ApJ, 555, 92
Marassi, S., Schneider, R., Limongi, M., & Chieffi, A. 2014, in Proc. Science, The Life Cycle of Dust in the Universe: Observations, Theory, and Laboratory Experiments, ed. A. Anderson, M. Baes, H. Gomez, C. Kemper, & D. Watson, http://pos.sissa.it/cgi-bin/reader/conf.cgi?confid=207, id.89
Masseron, T., Johnson, J. A., Plez, B., et al. 2010, A&A, 509, 93
Meynet, G., Ekström, S., & Maeder, A. 2006, A&A, 447, 623
Meynet, G., Hirschi, R., Ekstrom, S., et al. 2010, A&A, 521, A30
Norris, J. E., Christlieb, N., Korn, A. J., et al. 2007, ApJ, 670, 774
Norris, J. E., Yong, D., Bessell, M. S., et al. 2013, ApJ, 762, 28
Nozawa, T., & Kozasa, T. 2003, ApJ, 598, 785
Nozawa, T., & Kozasa, T. 2013, ApJ, 776, 24
Nozawa, T., Kozasa, T., Habe, A., et al. 2007, ApJ, 666, 955
Nozawa, T., Kozasa, T., & Nomoto, K. 2012, ApJL, 756, 35L
Nozawa, T., Kozasa, T., Tominaga, N., et al. 2010, ApJ, 713, 356
Omukai, K. 2000, ApJ, 534, 809
Omukai, K., Tsuribe, T., Schneider, R., & Ferrara, A. 2005, ApJ, 626, 627
Paquette, J. A., & Nuth, J. A., III. 2011, ApJL, 737, L6
Sarangi, A., & Cherchneff, I. 2013, ApJ, 776, 107
Schneider, R., Ferrara, A., & Salvaterra, R. 2004, MNRAS, 351, 1379
Schneider, R., Ferrara, A., Salvaterra, R., Omukai, K., & Bromm, V. 2003, Natur, 422, 869
Schneider, R., & Omukai, K. 2010, MNRAS, 402, 429
Schneider, R., Omukai, K., Bianchi, S., & Valiante, R. 2012a, MNRAS, 419, 1566
Schneider, R., Omukai, K., Limongi, M., et al. 2012b, MNRAS, 423, L60
Schneider, R., Valiante, R., Ventura, P., et al. 2014, MNRAS, 442, 1440
Silvia, D. W., Smith, B. D., & Shull, J. M. 2010, ApJ, 715, 1575
Silvia, D. W., Smith, B. D., & Shull, J. M. 2012, ApJ, 748, 12
Suda, T., Aikawa, M., Machida, M. N., Fujimoto, M. Y., & Iben, I. J. 2004, ApJ, 611, 476
Tanaka, K. E. I., & Omukai, K. 2014, MNRAS, 439, 1884
Todini, P., & Ferrara, A. 2001, MNRAS, 325, 726
Tominaga, N., Umeda, H., & Nomoto, K. 2007, ApJ, 660, 516
Truelove, J. K., & McKee, C. F. 1999, ApJ, 120, 299
Umeda, H., & Nomoto, K. 2002, ApJ, 565, 385
Umeda, H., & Nomoto, K. 2003, Natur, 422, 871
UMIST datatbase for astrochemistry. 2012, http://udfa.ajmarkwick.net
Valiante, R., & Schneider, R. 2014, in Proc. Science, The Life Cycle of Dust in the Universe: Observations, Theory, and Laboratory Experiments, ed. A. Anderson, M. Baes, H. Gomez, C. Kemper, & D. Watson, http://pos.sissa.it/cgi-bin/reader/conf.cgi?confid=207, id.12
Yong, D., Norris, J. E., Bessell, M. S., et al. 2013a, ApJ, 762, 26
Yong, D., Norris, J. E., Bessell, M. S., et al. 2013b, ApJ, 762, 27